



Second-order transient-extracting transform for the analysis of impulsive-like signals

Gang Yu ^{a,*}, Tian Ran Lin ^{b,*}

^a School of Electrical Engineering, University of Jinan, Jinan 250022, China

^b School of Mechanical and Automotive Engineering, Qingdao University of Technology, Qingdao 266520, PR China



ARTICLE INFO

Article history:

Received 16 October 2019

Received in revised form 17 May 2020

Accepted 11 June 2020

Keywords:

Time-frequency analysis

Bearing fault diagnosis

Transient-extracting transform

Synchrosqueezing transform

ABSTRACT

In this paper, a high resolution time–frequency analysis method, termed as second-order transient-extracting transform (STET) is proposed in the analysis of highly non-stationary signals with strong impulse components for machine fault diagnosis. The limitation of two recently published post-processing techniques are discussed and highlighted based on a theoretical analysis of the first and the second-order frequency-varying models. A STET technique is then proposed to overcome this limitation. The discrete implementation of STET is also presented in the study and the performance of the technique is examined by a number of simulated numerical data and three sets of experimental data. The results confirm the effectiveness of the proposed technique in the analysis of noise contaminated signals as well as bearing defect signals acquired under varying speed condition.

© 2020 Elsevier Ltd. All rights reserved.

1. Introduction

Rolling element bearing plays an important role in rotating machinery such as wind turbines, aero-engines and high-speed trains. Unfortunately, bearing failure is one of the most frequently reported reasons for machine breakdown, and a great effort has been devoted by researchers and engineers to prevent such occurrences. Vibration-based condition-monitoring (CM) is one of the most effective non-intrusive technique for the detection of a bearing defect, which has been widely employed by practitioners in the last few decades [1,2]. When a rolling element passes through a defective surface or when a defective element rolls on a race surface, an impulse signal will be generated, and the signal is then amplified by the bearing resonance which can be captured by vibration sensors installed on the bearing house [3,4]. However, due to background noise and signal interference from other sources, a bearing defect, particularly incipient defect can often go undetected, which highlights the needs to develop effective signal processing techniques for an accurate and reliable bearing fault diagnosis.

A critical criterion of an effective bearing fault diagnosis program is that it can detect a defect information in an incipient stage even under the interference of machine operating noise. Various signal processing techniques have been developed to serve this purpose, which can be generally divided into three categories, e.g. time domain analysis, frequency domain analysis and time–frequency (TF) analysis (TFA) techniques. TFA technique has been well employed in machine fault diagnosis due to its ability in dealing with non-stationary CM signals caused by changing load or operating speed conditions [5–8].

* Corresponding authors.

E-mail addresses: yugang2010@163.com (G. Yu), trlin888@163.com (T.R. Lin).

Short-time Fourier transform (STFT) and wavelet transform (WT) are two mostly employed conventional TFA techniques in machine fault diagnosis. Both techniques belong to the linear TFA category which characterize the TF feature by calculating the inner product between a signal and a series of TF basis functions [9,10]. However, the basis functions designed in the linear TFA technique are implicitly assumed to be stationary or quasi-stationary in the analyzed timeframe which then restricts the application of the technique in dealing with signals having a rapid changing dynamic. To overcome such shortcoming, several non-linear TFA techniques were proposed in recent years. For instance, linear chirplet transform [11], local polynomial transform [12], polynomial chirplet transform (PCT) [9], parameterized TF transform [10] and matching demodulation transform [13] are some of these recent attempts. All these methods aim to construct new basis functions based on the non-linearity of the analyzed signal. The newly designed basis function performs better in the analysis of non-stationary signals than the linear basis function, though it will have the same limitation when the non-linearity of a signal increases. This is because that the non-linearity of a practical signal is difficult to predict or estimate in advance. Moreover, due to the Heisenberg uncertainty principle, these existing non-linear TFA techniques often suffer from the diffused TF energy problem.

Recently, the new trend in the development of TFA techniques is to characterize the non-linear features of a non-stationary signal using post-processing procedures, such as reassignment method (RM) [14,15], synchrosqueezing transform [16,17] (SST) and synchroextracting transform (SET) [18-21]. It is well known from the Heisenberg uncertainty principle that the TF representation (TFR) generated by a linear TFA technique usually smears around the instantaneous frequency (IF) trajectory of the signal. To overcome this problem, the RM technique reassigns the diffused TF energy into the IF trajectory in both time and frequency axes [14], which then produces a higher energy concentrated TFR in the TF plane. However, a drawback of RM is that the TF result cannot be used for signal reconstruction. In contrast, because SST technique only reassigns the TF coefficients in the frequency direction [16], it retains the reconstruction ability of the TF result. Although the TF resolution of the SST is not higher than that of the RM, the practical application of the SST is much more general due to its reversibility. Moreover, with the development of high-order SST, it has been proved that SST analysis can achieve a better resolution than RM [22,23]. The drawback of SST is that it lacks the capacity to remove the noise interference when a signal is contaminated by noise. This is because that the post-processing procedure of SST may reassign the noise into the eventual TFR. To address this issue, SET, a recently proposed technique can retain the most-related TF coefficients and discard the weak-related TF coefficients to suppress the noise interference [18].

Several recently published works utilizing SST or SET technique and combined them with other non-linear TFA methods to further improve the performance of SST and SET techniques. For instance, Wang et al first constructed an iterative TFA transform to demodulate a non-linear signal with good energy concentration, and then reassigned the corresponding TF coefficients using SST to enhance the TF resolution [13]. Shi et al proposed a generalized stepwise demodulation transform to come along with SST [24]. Tu et al introduced a demodulated SST to deal with a fast varying vibration signal [5]. Yu et al combined a PCT with SET to capture the changing dynamic in non-stationary signals [25].

For both SST and SET, they analyze a signal by assuming that the IF of the signal can be locally approximated as a time unvarying segment in the analyzed window frame. SST and SET have also been expanded into high-order polynomial models for the analysis of more complex signals. In theory, such high-order methods have a better ability to deal with signals containing strong time-varying modes. For example, Oberlin et al proposed a concentrated SST technique by defining a precise IF estimate for a second-order frequency-modulated signal [22]. Wang et al introduced an improved SST by constructing an IF estimate to precisely match the characteristic of a fast varying signal [3]. Pham et al put forward a generalized SST using a higher-order estimate of IF [23]. Hu et al proposed a higher-order SST based on WT [26]. Whilst Yu et al employed a fix point iteration algorithm to progressively improve the TF resolution of SST [27].

However, an impulsive-like signal cannot be well approximated by a time-varying model since the impulses generated by a defect usually occurs in a very short time duration and has a broadband frequency. This implies that the time-varying assumption made by the above TFA techniques does not fit well to characterize a signal produced by a bearing fault. A couple of recently published techniques such as time-reassigned SST [28] and transient-extracting transform (TET) [29] which used alternative frequency-varying models were proposed in an attempt to overcome the limitation of time-varying models used in the above-mentioned TFA techniques in the analysis of impulsive-like signals. However, these two techniques are not adequate in the analysis of more complex signals since they are established based on first-order models. To overcome this problem, an energy concentrated TFA using a second-order frequency-varying model and based on TET framework is proposed in this paper for the analysis of impulsive-like signals.

The remainder of this paper is organized as follows. In Section 2, the theoretical basis of TSST and TET methods are reviewed based on Dirac delta function and a second-order frequency-varying model. Section 3 provides a detailed layout and elaboration of the proposed method. Numerical and experimental validations are given in Section 4 and Section 5, respectively. Conclusions are drawn in Section 6.

2. A review of the theoretical basis of TSST and TET techniques

2.1. A theoretical background of TSST and TET

TSST and TET are proposed as the post-processing tools of STFT given by Eq. (1).

$$G(t, \omega) = \int_{-\infty}^{+\infty} g(u-t)s(u)e^{-i\omega u} du. \quad (1)$$

where $g(u-t)$ is the sliding window function and $\text{supp}(g) \in [-\Delta, \Delta]$. An impulsive-like signal often occurs in a very short time duration, thus, Dirac delta function can be the ideal model to describe such a signal. To start with, let's first consider the analysis of an impulse signal given in Eq. (2) using STFT,

$$s(t) = A\delta(t-t_0) \quad (2)$$

where A is the amplitude of the impulse signal which occurs at the time instant t_0 . Substituting Eq. (2) into Eq. (1) to have

$$G(t, \omega) = Ag(t_0-t)e^{-i\omega t_0} \quad (3)$$

Considering that the window $g(t)$ is compactly supported in the region $t \in [-\Delta, \Delta]$, the STFT result of the Dirac delta function should spread around the line $t = t_0$. Refs. [28,29] used a two-dimensional (2D) group delay (GD) estimate to reallocate the diffused energy of STFT of the signal, which is written as

$$\hat{t}(t, \omega) = \text{Re}\left(\frac{i\partial_\omega G(t, \omega)}{G(t, \omega)}\right). \quad (4)$$

where $\text{Re}(\cdot)$ denotes the real part. Substituting Eq. (3) into Eq. (4) to have the following expression,

$$\hat{t}(t, \omega) = t_0. \quad (5)$$

Eq. (5) means that the 2D GD estimate of the Dirac delta function calculated using Eq. (4) is consistent with the occurring time instant of the impulse. Inspired by this property, TSST and TET consider two strategies respectively to improve the TF resolution of STFT. The expression of TSST is given by

$$Ts(u, \omega) = \int_{-\infty}^{+\infty} G(t, \omega)\delta(u-\hat{t}(t, \omega))dt. \quad (6)$$

It is shown in Eq. (6) that TSST employs an operator $\int_{-\infty}^{+\infty} \delta(u-\hat{t}(t, \omega))dt$ to reassign the diffused STFT result into the occurring time instant of the impulse. Whilst according to Ref. [29], the expression of the TET is given in Eq. (7).

$$Te(t, \omega) = G(t, \omega)\delta(t-\hat{t}(t, \omega)). \quad (7)$$

Eq. (7) shows that TET uses a SET-like operator $\delta(t-\hat{t}(t, \omega))$ to retain only the TF coefficients at the time instant t_0 while discarding the weakly-related TF coefficients. Combining Eq. (6) and Eq. (7), we can further derive the following expression:

$$(\hat{g}(0))^{-1}Ts(t, \omega) = (g(0))^{-1}Te(t, \omega) = Ae^{-i\omega t_0}\delta(t-t_0) \quad (8)$$

where $\hat{g}(\cdot)$ denotes the Fourier transform of the sliding window function. Eq. (8) demonstrates that both TSST and TET have the same ability to achieve a higher TF resolution for a noise-free impulsive-like signal. However, it is noted that TET algorithm is more effective in capturing the TF feature in the signal using the operator $\delta(t-\hat{t}(t, \omega))$ for a noise-contaminated signal. This is because that the noise can spread in the entire TF plane and the reassignment procedure used by TSST will unavoidably reassign both signal and noise into the TFR. On the contrary, the post-processing operator of TET can remove both weakly-related TF coefficients and noise at the same time leading to the well desired noise-suppression property of TET technique.

A numerical example is given in the following text to further illustrate the performance of TSST and TET. In this example, a discrete delta function is modelled as $s(n) = \delta(n-0.5)$, which is sampled using a 200 Hz sampling frequency as shown in Fig. 1(a). The STFT result of the signal is displayed in Fig. 1(b) where the TF energy of this signal is found to smear around the time instant at 0.5 s. The corresponding TSST and TET results are shown in Fig. 1(c-d). It is shown that both methods can effectively produce an energy concentrated and high resolution TF result of the signal, which is consistent with the above theoretical analysis. A Gaussian white noise is then added onto this signal as shown in Fig. 2(a). The STFT, TSST and TET results of the noise-added signal are shown in Fig. 2(b-d) respectively. Once again, both TSST and TET methods produce higher energy concentrated TFRs than that of STFT. However, the TF feature of the TSST result is not as prominent as that of the TET result due to noise interference. The result confirms the theoretical discussion presented in the previous text.

2.2. The limitation of TET

In this section, a theoretical analysis of TET when dealing with first and second-order frequency-varying model signals is presented. A frequency-varying model described by Eq. (9) is used to analyze the theoretical performance of TET.

$$\hat{s}(\omega) = A(\omega)e^{i\varphi(\omega)}. \quad (9)$$

where $\hat{s}(\omega)$ denotes the Fourier transform of the signal, $A(\omega)$ and $\varphi(\omega)$ are the signal amplitude and phase in the frequency domain and the parameter $-\varphi'(\omega)$ is the GD of the signal. For the Dirac delta function, a more general mathematic model can

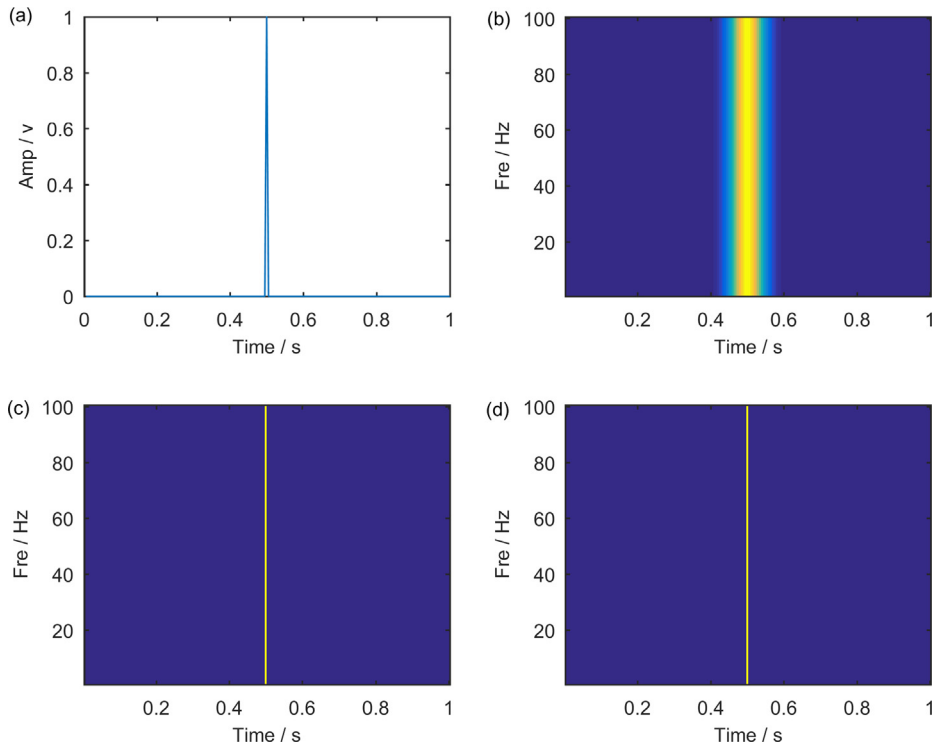


Fig. 1. (a) Dirac delta function signal, (b) STFT result, (c) TSST result and (d) TET result.

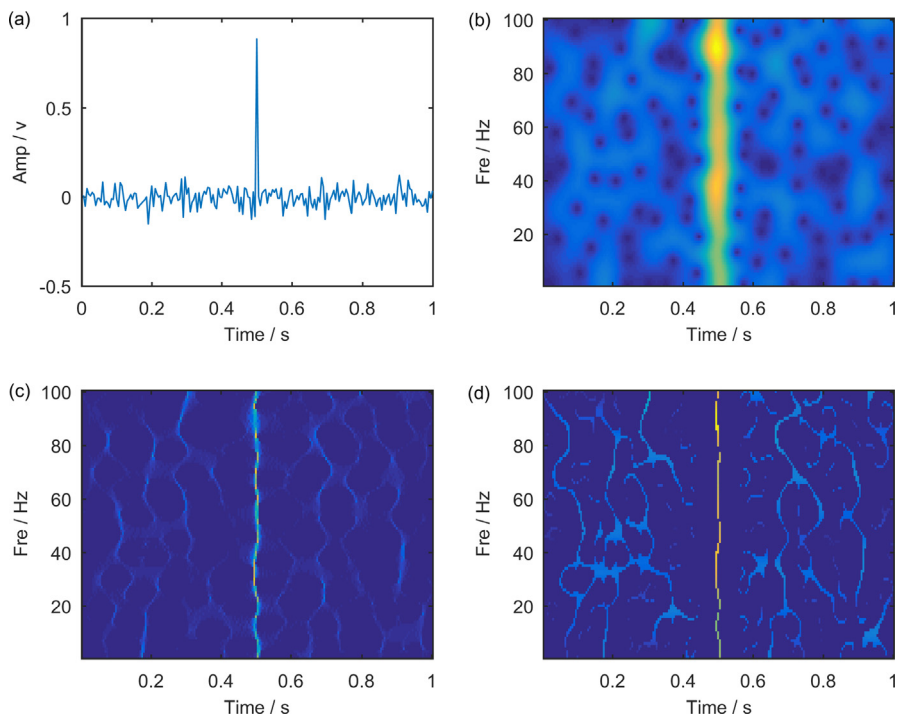


Fig. 2. (a) Dirac delta function signal added with noise, (b) STFT result, (c) TSST result and (d) TET result.

be obtained by assuming that $\exists \varepsilon$ is sufficient small, $|A'(\omega)| \leq \varepsilon$ and $|\varphi''(\omega)| \leq \varepsilon$ for $\forall \omega$. Then the frequency-varying model of the Dirac delta function can be re-expressed as

$$\hat{s}(\xi) = A(\omega)e^{i(\varphi(\omega)+\varphi'(\omega)(\xi-\omega))}. \quad (10)$$

Eq. (10) is the first-order expansion of the signal given in Eq. (9), which is often termed as the first-order frequency-varying model. To analyze this model, the STFT expression in frequency domain is needed, which can be written as

$$G(t, \omega) = (2\pi)^{-1} \int_{-\infty}^{+\infty} \hat{s}(\xi)\hat{g}(\xi - \omega)e^{i(\xi-\omega)t}d\xi. \quad (11)$$

where $\hat{g}(\omega)$ denotes the Fourier transform of the window function $g(t) = e^{-(2\sigma)^{-1}t^2}$ and $\hat{g}(\omega) = \sqrt{2\sigma\pi}e^{-0.5\sigma\omega^2}$. Substituting Eq. (10) into Eq. (11) to derive

$$\begin{aligned} G(t, \omega) &= (2\pi)^{-1}A(\omega)e^{i\varphi(\omega)} \int_{-\infty}^{+\infty} e^{i(t+\varphi'(\omega))(\xi-\omega)}\hat{g}(\xi - \omega)d\xi \\ &= A(\omega)e^{i\varphi(\omega)}g(t + \varphi'(\omega)) \\ &= A(\omega)e^{i\varphi(\omega)}e^{-\frac{(t+\varphi'(\omega))^2}{2\sigma}}. \end{aligned} \quad (12)$$

Substituting Eq. (12) into Eq. (4) to have the following equation,

$$\hat{t}(t, \omega) = -\varphi'(\omega). \quad (13)$$

Eq. (13) demonstrates that Eq. (4) can provide an exact estimate for the GD of the first-order frequency-varying signal. Based on the above analysis, the TET result of the signal given in Eq. (10) can be derived as

$$\begin{aligned} Te(t, \omega) &= A(\omega)e^{i\varphi(\omega)}e^{-(2\sigma)^{-1}(t+\varphi'(\omega))^2}\delta(t - \hat{t}(t, \omega)) \\ &= A(\omega)e^{i\varphi(\omega)}\delta(t + \varphi'(\omega)). \end{aligned} \quad (14)$$

The result given by Eq. (14) leads to the same conclusion as that from the Eq. (7). Furthermore, the TET result can also be used for the following signal reconstruction [29],

$$\hat{s}(\omega) = Te(-\varphi'(\omega), \omega). \quad (15)$$

In discrete data processing, Eq. (14) is often implemented by the following expression

$$Te(n, k) = \begin{cases} G(n, k), & \text{if } |n + \varphi'(k)| < \frac{\Delta n}{2} \\ 0, & \text{otherwise} \end{cases} \quad (16)$$

where n, k and Δn denote the discrete time variable, frequency variable and the sampling time interval respectively. It is shown from Eq. (16) that TET retains the TF coefficients of the STFT result in the TF region $n \in (-\varphi'(k) - 0.5 \Delta n, -\varphi'(k) + 0.5 \Delta n)$. Whilst the TF coefficients in the TF region $n \notin (-\varphi'(k) - 0.5 \Delta n, -\varphi'(k) + 0.5 \Delta n)$ is discarded.

To further explore the property of TET, a second-order frequency-varying model is established in the following analysis by the assumption that, $\exists \varepsilon$ is sufficient small, $|A'(\omega)| \leq \varepsilon$ and $|\varphi'''(\omega)| \leq \varepsilon$ for $\forall \omega$. As a result, the signal given by Eq. (9) can be rewritten as

$$\hat{s}(\xi) = A(\omega)e^{i(\varphi(\omega)+\varphi'(\omega)(\xi-\omega)+0.5\varphi''(\omega)(\xi-\omega)^2)}. \quad (17)$$

Now substituting Eq. (17) into Eq. (11) to have

$$\begin{aligned} G(t, \omega) &= (2\pi)^{-1} \int_{-\infty}^{+\infty} A(\omega)e^{i(\varphi(\omega)+\varphi'(\omega)(\xi-\omega)+0.5\varphi''(\omega)(\xi-\omega)^2)}\sqrt{2\sigma\pi}e^{-\frac{\sigma(\xi-\omega)^2}{2}}e^{i(\xi-\omega)t}d\xi \\ &= \sqrt{2\sigma\pi}A(\omega)e^{i\varphi(\omega)}(2\pi)^{-1} \int_{-\infty}^{+\infty} e^{0.5(i\varphi''(\omega)-\sigma)(\xi-\omega)^2}e^{i(t+\varphi'(\omega))(\xi-\omega)}d\xi \\ &= A(\omega)e^{i\varphi(\omega)}\sqrt{\frac{\sigma}{\sigma-i\varphi''(\omega)}}e^{\frac{(t+\varphi'(\omega))^2}{2\sigma-2i\varphi''(\omega)}}. \end{aligned} \quad (18)$$

From Eq. (4), the 2D GD estimate of Eq. (18) can be derived

$$\hat{t}(t, \omega) = -\varphi'(\omega) + \frac{\varphi''(\omega)^2}{\sigma^2 + \varphi''(\omega)^2}(t + \varphi'(\omega)). \quad (19)$$

From Eq. (19), the TET result of the second-order frequency-varying model can be deduced as

$$\begin{aligned} Te(t, \omega) &= G(t, \omega)\delta(t - \hat{t}(t, \omega)) \\ &= G(t, \omega)\delta\left(t + \varphi'(\omega) - \frac{\varphi''(\omega)^2}{\sigma^2 + \varphi''(\omega)^2}(t + \varphi'(\omega))\right) \\ &= G(t, \omega)\delta\left(\frac{\sigma^2}{\sigma^2 + \varphi''(\omega)^2}(t + \varphi'(\omega))\right). \end{aligned} \quad (20)$$

The discrete implementation of Eq. (20) is

$$Te(n, k) = \begin{cases} G(n, k), & \text{if } \left| \frac{\sigma^2}{\sigma^2 + \varphi''(k)^2} (n + \varphi'(k)) \right| < \frac{\Delta n}{2} \\ 0, & \text{otherwise.} \end{cases} \quad (21)$$

From Eq. (21), it becomes obvious that the TET result described by Eq. (17) can retain the STFT result in the TF region $n \in (-\varphi'(k) - \sigma^{-2}(\sigma^2 + \varphi''(k)^2)0.5 \Delta n, -\varphi'(k) + \sigma^{-2}(\sigma^2 + \varphi''(k)^2)0.5 \Delta n)$. Comparing Eq. (16) with Eq. (21), it is found that the TET result of the second-order frequency-varying signal is less energy concentrated than that of the first-order frequency-varying signal. Moreover, following an increase of $\varphi''(k)$, the TET result will be more diffused. Therefore, it can be concluded that TET technique will not perform well in dealing with signals having the second-order frequency-varying characteristic.

3. Second-order transient-extracting transform (STET)

3.1. The theoretical derivation of STET

To construct an improved TET for the analysis of the signal described by Eq. (17), we first derive the following expression according to Eq. (19)

$$-\varphi'(\omega) = \frac{\sigma^2 + \varphi''(\omega)^2}{\sigma^2} \left(\hat{t}(t, \omega) - \frac{t\varphi''(\omega)^2}{\sigma^2 + \varphi''(\omega)^2} \right). \quad (22)$$

Eq. (22) provides an indication of how to calculate the new 2D GD estimate in the analysis of a second-order signal. To achieve this purpose, we first define a novel 2D estimate $\hat{\omega}(t, \omega)$ given by

$$\hat{\omega}(t, \omega) = \text{Re} \left(\frac{\partial_t G(t, \omega)}{G(t, \omega)} \right) = -\frac{\sigma(t + \varphi'(\omega))}{\sigma^2 + \varphi''(\omega)^2}. \quad (23)$$

For the estimates $\hat{t}(t, \omega)$ and $\hat{\omega}(t, \omega)$, we respectively calculate the partial derivative of them with respect to time and frequency. The related expressions are listed in Eqs. (24–27).

$$\partial_t \hat{t}(t, \omega) = \frac{\varphi''(\omega)^2}{\sigma^2 + \varphi''(\omega)^2}. \quad (24)$$

$$\partial_\omega \hat{t}(t, \omega) = -\frac{\sigma^2 \varphi''(\omega)}{\sigma^2 + \varphi''(\omega)^2}. \quad (25)$$

$$\partial_t \hat{\omega}(t, \omega) = -\frac{\sigma}{\sigma^2 + \varphi''(\omega)^2}. \quad (26)$$

$$\partial_\omega \hat{\omega}(t, \omega) = -\frac{\sigma \varphi''(\omega)}{\sigma^2 + \varphi''(\omega)^2}. \quad (27)$$

Inspired by Eq. (22), the following expression can now be constructed,

$$\hat{t}^{[2]}(t, \omega) = -\frac{\partial_\omega \hat{\omega}(t, \omega)}{\partial_t \hat{\omega}(t, \omega) \partial_\omega \hat{t}(t, \omega)} (\hat{t}(t, \omega) - t \partial_t \hat{t}(t, \omega)). \quad (28)$$

where the superscript [2] indicates a second-order estimate. Substituting Eqs. (24–27) into Eq. (22), we can derive the following

$$\hat{t}^{[2]}(t, \omega) = -\varphi'(\omega) \quad (29)$$

Eq. (29) confirms that an exact 2D GD estimate for the second-order frequency-varying model can be obtained. However, to construct the 2D GD estimate given by Eq. (28), it is necessary to ensure that $|\partial_t \hat{\omega}(t, \omega) \partial_\omega \hat{t}(t, \omega)| \neq 0$. Therefore, a modified 2D GD estimate of the second-order model is given below

$$\hat{t}^{[2]}(t, \omega) = \begin{cases} -\frac{\partial_\omega \hat{\omega}(t, \omega)}{\partial_t \hat{\omega}(t, \omega) \partial_\omega \hat{t}(t, \omega)} (\hat{t}(t, \omega) - t \partial_t \hat{t}(t, \omega)) & \text{if } |\partial_t \hat{\omega}(t, \omega) \partial_\omega \hat{t}(t, \omega)| > 1^{-10} \\ \hat{t}(t, \omega) & \text{otherwise} \end{cases}. \quad (30)$$

It is shown from the above analysis that, for the second-order model, the $\hat{t}^{[2]}(t, \omega)$ can achieve a better estimate than the $\hat{t}(t, \omega)$. However, apart from the GD estimate, it is also necessary to rectify the amplitude of the STFT result given by Eq. (18). For this purpose, we first calculate the STFT in the GD trajectory $t = -\varphi'(\omega)$, i.e.

$$\begin{aligned} G(-\varphi'(\omega), \omega) &= A(\omega)e^{i\varphi(\omega)}\sqrt{\frac{\sigma}{\sigma-i\varphi''(\omega)}} \\ &= A(\omega)e^{i\varphi(\omega)}\sqrt{\frac{\sigma^2}{\sigma^2+\varphi''(\omega)^2}+i\frac{\sigma\varphi''(\omega)}{\sigma^2+\varphi''(\omega)^2}} \\ &= A(\omega)e^{i\varphi(\omega)}\sqrt{-\frac{\partial_t\hat{\omega}(t,\omega)\partial_\omega\hat{t}(t,\omega)}{\partial_\omega\hat{\omega}(t,\omega)}-i\partial_\omega\hat{\omega}(t,\omega)} \end{aligned} \tag{31}$$

Inspired by Eq. (31), a rectified STFT $G^{[2]}(t, \omega)$ can be constructed using

$$G^{[2]}(t, \omega) = \frac{G(t, \omega)}{\sqrt{-\frac{\partial_t\hat{\omega}(t,\omega)\partial_\omega\hat{t}(t,\omega)}{\partial_\omega\hat{\omega}(t,\omega)}-i\partial_\omega\hat{\omega}(t,\omega)}} \tag{32}$$

Combing Eq. (32) with Eq. (30), a modified $G^{[2]}(t, \omega)$ for the second-order frequency-varying signal can be calculated as

$$G^{[2]}(t, \omega) = \begin{cases} \frac{G(t, \omega)}{\sqrt{-\frac{\partial_t\hat{\omega}(t,\omega)\partial_\omega\hat{t}(t,\omega)}{\partial_\omega\hat{\omega}(t,\omega)}-i\partial_\omega\hat{\omega}(t,\omega)}} & \text{if } |\partial_t\hat{\omega}(t, \omega)\partial_\omega\hat{t}(t, \omega)| > 1^{-10} \\ G(t, \omega) & \text{otherwise} \end{cases} \tag{33}$$

Finally, an improved TET, termed as the second-order TET (STET) can be obtained as

$$Te^{[2]}(t, \omega) = G^{[2]}(t, \omega)\delta(t - \hat{t}^{[2]}(t, \omega)). \tag{34}$$

Substituting Eq. (29) and Eq. (32) into Eq. (34), the STET of the signal given by Eq. (17) can be derived as

$$Te^{[2]}(t, \omega) = A(\omega)e^{i\varphi(\omega)}\delta(t + \varphi'(\omega)). \tag{35}$$

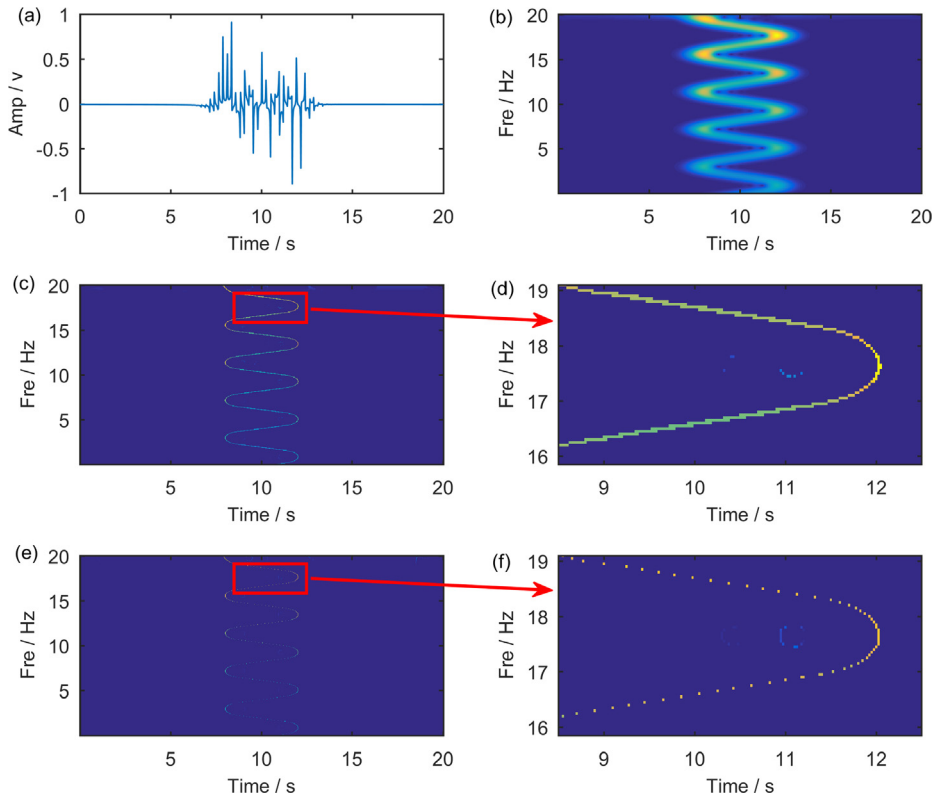


Fig. 3. (a) The time waveform of the signal given in Eq. (36), (b) STFT result, (c) TET result, (d) zoomed version of the TET result, (e) STET result and (f) zoomed version of the STET result.

Eq. (35) illustrates that the proposed STET can generate a high-resolution TFR for the second-order frequency-varying signal. A numerical model of a frequency-varying signal is given below to exemplify the enhancement of STET when comparing with TET

$$\hat{s}(\omega) = e^{0.05\omega} e^{-i(10\omega + 1.5\sin(1.5\omega))} \tag{36}$$

where the sampling frequency and the sampling time are 40 Hz and 20 s respectively. The time domain waveform of the signal and the STFT result are plotted in Fig. 3(a-b). It is observed that the TF energy of the STFT result diffuses around the GD trajectory where there are multiple frequency points for each time instant. For comparison, the TET and STET results are displayed in Fig. 3(c-f). It is obvious that TET and STET can achieve a better energy concentrated TFR than STFT. It is further shown in the zoomed version that the proposed STET can generate a better TF representation than that of TET. This confirms that STET possesses a better capacity to characterize the TF feature of a strong frequency-varying signal than TET.

Computational efficiency is an important indicator for the effectiveness of a TFA algorithm. To test the efficiency of the algorithm, the execution time of the proposed algorithm is compared to that of some well employed TFA algorithms. The configurations of the computer used in the simulation are: A laptop computer having an Intel Core i7-6500 2.5 GHz CPU, 8.0 GB of DDR3 RAM, operated based on a Window 10 OS system, and the code is executed using MATLAB R2016a. The execution times of various algorithms are listed in Table 1 for comparison. The result shows that the execution time of the proposed algorithm for the analysis of the signal described by Eq. (36) is 0.39 s, which is not too much different than that of other algorithms.

3.2. The implementation of STET

In this section, we focus mainly on the algorithm implementation of STET, where $\hat{t}(t, \omega)$ and its partial derivative are considered first. Based on Eq. (4), the parameter $\partial_\omega G(t, \omega)$ can be obtained by

$$\begin{aligned} \partial_\omega G(t, \omega) &= -i \int_{-\infty}^{+\infty} g(u-t)s(u)ue^{-i\omega u} du \\ &= -iG_{su}(t, \omega) \end{aligned} \tag{37}$$

Thus, the $\hat{t}(t, \omega)$ can also be obtained by

$$\hat{t}(t, \omega) = \text{Re} \left(\frac{G_{su}(t, \omega)}{G(t, \omega)} \right). \tag{38}$$

Moreover, the derivative of the $\hat{t}(t, \omega)$ with respect to time and frequency can be derived by Eq. (39) and Eq. (40), respectively.

$$\begin{aligned} \partial_t \hat{t}(t, \omega) &= \text{Re} \left(\partial_t \left(\frac{G_{su}(t, \omega)}{G(t, \omega)} \right) \right) \\ &= \text{Re} \left(\frac{-t \int_{-\infty}^{+\infty} g'(u-t)s(u)ue^{-i\omega u} du G(t, \omega) + G_{su}(t, \omega) t \int_{-\infty}^{+\infty} g'(u-t)s(u)e^{-i\omega u} du}{(G(t, \omega))^2} \right) \\ &= \text{Re} \left(\frac{-tG_{su}g'(t, \omega)G(t, \omega) + G_{su}(t, \omega)tG^g(t, \omega)}{(G(t, \omega))^2} \right) \end{aligned} \tag{39}$$

where $g'()$ denotes the derivative of the window function with respect to the time variable.

$$\begin{aligned} \partial_\omega \hat{t}(t, \omega) &= \text{Re} \left(\partial_\omega \left(\frac{G_{su}(t, \omega)}{G(t, \omega)} \right) \right) \\ &= \text{Re} \left(\frac{-i \int_{-\infty}^{+\infty} g(u-t)s(u)u^2 e^{-i\omega u} du G(t, \omega) + i(G_{su}(t, \omega))^2}{(G(t, \omega))^2} \right) \\ &= \text{Re} \left(\frac{-iG_{su}^2(t, \omega)G(t, \omega) + i(G_{su}(t, \omega))^2}{(G(t, \omega))^2} \right) \end{aligned} \tag{40}$$

To obtain $\hat{\omega}(t, \omega)$, we first calculate $\partial_t G(t, \omega)$ in Eq. (23).

$$\partial_t G(t, \omega) = - \int_{-\infty}^{+\infty} g'(u-t)s(u)e^{-i\omega u} du = -G^g(t, \omega). \tag{41}$$

The $\hat{\omega}(t, \omega)$ can now be obtained as

Table 1
A comparison of the execution times using different algorithms.

Algorithm	STFT	TET	TSST	STET
Time (s)	0.055	0.177	0.428	0.39

$$\hat{\omega}(t, \omega) = \operatorname{Re}\left(-\frac{G^{g'}(t, \omega)}{G(t, \omega)}\right) \tag{42}$$

Furthermore, the derivative of $\hat{\omega}(t, \omega)$ with respect to time and frequency can be derived from Eq. (43) and Eq. (44) respectively.

$$\begin{aligned} \partial_t \hat{\omega}(t, \omega) &= \operatorname{Re}\left(-\frac{\partial_t G^{g'}(t, \omega)G(t, \omega) - G^{g'}(t, \omega)\partial_t G(t, \omega)}{(G(t, \omega))^2}\right) \\ &= \operatorname{Re}\left(\frac{G^{g''}(t, \omega)G(t, \omega) - (G^{g'}(t, \omega))^2}{(G(t, \omega))^2}\right) \end{aligned} \tag{43}$$

where $\partial_t G^{g'}(t, \omega) = -\int_{-\infty}^{+\infty} g''(u-t)s(u)e^{-i\omega u} du = -G^{g''}(t, \omega)$ and $g''()$ denotes the second-order derivative of the window function with respect to the time variable.

$$\begin{aligned} \partial_\omega \hat{\omega}(t, \omega) &= \operatorname{Re}\left(-\frac{\partial_\omega G^{g'}(t, \omega)G(t, \omega) - G^{g'}(t, \omega)\partial_\omega G(t, \omega)}{(G(t, \omega))^2}\right) \\ &= \operatorname{Re}\left(\frac{iG_{su}^{g'}(t, \omega)G(t, \omega) - iG^{g'}(t, \omega)G_{su}(t, \omega)}{(G(t, \omega))^2}\right) \end{aligned} \tag{44}$$

At the beginning of this section, the Gaussian window function $g(t) = e^{-(2\sigma)^{-1}t^2}$ is used in the analysis. The derivative of the window function, i.e. $g'(t)$ and $g''(t)$ in the above equations can also be obtained that $g'(t) = -(\sigma)^{-1}te^{-(2\sigma)^{-1}t^2}$ and $g''(t) = \sigma^{-2}(t^2 - \sigma^2)e^{-(2\sigma)^{-1}t^2}$. Finally, the $G_{su}(t, \omega)$, $G_{su}^{g'}(t, \omega)$, $G^{g'}(t, \omega)$, $G_{su^2}(t, \omega)$ and $G^{g''}(t, \omega)$ in the above analysis can be calculated using the alternative STFTs to be presented in the following text.

Now, the discrete implementation of the STET can be presented based on the above analysis. Letting $s[n]$ denotes the discrete version of a time-series signal, $n = 0, 1, \dots, N-1$, where N is the number of samples, and the data $s[n]$ corresponds to a uniform discretization of the signal taken at the time instant $t_n = t_0 + nT$, where T is the sampling interval. The Fourier transform of data $s[n]$ is calculated by $S[k] = \sum_{n=0}^{N-1} s[n]e^{-i\frac{2\pi}{N}nk}$, where $k = 0, 1, \dots, N-1$. Letting $G[n, k]$, $G_{su}[n, k]$, $G_{su}^{g'}[n, k]$, $G^{g'}[n, k]$, $G_{su^2}[n, k]$ and $G^{g''}[n, k]$ denote the discrete version of the $G(t, \omega)$, $G_{su}(t, \omega)$, $G_{su}^{g'}(t, \omega)$, $G^{g'}(t, \omega)$, $G_{su^2}(t, \omega)$ and $G^{g''}(t, \omega)$, these STFTs can then be expressed as

$$G[n, k] = \sum_{m=0}^{N-1} g[m-n]s[m]e^{-i\frac{2\pi}{N}mk}. \tag{45}$$

$$G_{su}[n, k] = \sum_{m=0}^{N-1} g[m-n]s[m]me^{-i\frac{2\pi}{N}mk}. \tag{46}$$

$$G_{su}^{g'}[n, k] = \sum_{m=0}^{N-1} g'[m-n]s[m]me^{-i\frac{2\pi}{N}mk}. \tag{47}$$

$$G^{g'}[n, k] = \sum_{m=0}^{N-1} g'[m-n]s[m]e^{-i\frac{2\pi}{N}mk}. \tag{48}$$

$$G_{su^2}[n, k] = \sum_{m=0}^{N-1} g[m-n]s[m]m^2e^{-i\frac{2\pi}{N}mk}. \tag{49}$$

$$G^{g''}[n, k] = \sum_{m=0}^{N-1} g''[m-n]s[m]e^{-i\frac{2\pi}{N}mk}. \tag{50}$$

With these STFTs, the discrete $\hat{t}[n, k]$, $\partial_t \hat{t}[n, k]$, $\partial_\omega \hat{t}[n, k]$, $\hat{\omega}[n, k]$, $\partial_t \hat{\omega}[n, k]$ and $\partial_\omega \hat{\omega}[n, k]$ can be obtained by

$$\hat{t}[n, k] = \operatorname{Re}\left(\frac{G_{su}[n, k]}{G[n, k]}\right). \tag{51}$$

$$\partial_t \hat{t}[n, k] = \operatorname{Re}\left(\frac{-nG_{su}^{g'}[n, k]G[n, k] + G_{su}[n, k]nG^{g'}[n, k]}{(G[n, k])^2}\right). \tag{52}$$

$$\partial_\omega \hat{t}[n, k] = \operatorname{Re}\left(\frac{-iG_{su^2}[n, k]G[n, k] + i(G_{su}[n, k])^2}{(G[n, k])^2}\right). \tag{53}$$

$$\hat{\omega}[n, k] = \text{Re} \left(-\frac{G^{g'}[n, k]}{G[n, k]} \right). \tag{54}$$

$$\partial_t \hat{\omega}[n, k] = \text{Re} \left(\frac{G^{g''}[n, k]G[n, k] - (G^{g'}[n, k])^2}{(G[n, k])^2} \right). \tag{55}$$

$$\partial_\omega \hat{\omega}[n, k] = \text{Re} \left(\frac{iG_{su}^{g'}[n, k]G[n, k] - iG^{g'}[n, k]G_{su}[n, k]}{(G[n, k])^2} \right). \tag{56}$$

Furthermore, the $\hat{t}^{[2]}[n, k]$ and $G^{[2]}[n, k]$ can be calculated by

$$\hat{t}^{[2]}[n, k] = \begin{cases} -\frac{\partial_\omega \hat{\omega}[n, k]}{\partial_t \hat{\omega}[n, k] \partial_\omega \hat{t}[n, k]} (\hat{t}[n, k] - n \partial_t \hat{t}[n, k]) & \text{if } |\partial_t \hat{\omega}[n, k] \partial_\omega \hat{t}[n, k]| > 1^{-10} \\ \hat{t}[n, k] & \text{otherwise} \end{cases}. \tag{57}$$

$$G^{[2]}[n, k] = \begin{cases} \frac{G[n, k]}{\sqrt{\frac{\partial_t \hat{\omega}[n, k] \partial_\omega \hat{t}[n, k]}{\partial_\omega \hat{\omega}[n, k]} - i \partial_\omega \hat{\omega}[n, k]}} & \text{if } |\partial_t \hat{\omega}[n, k] \partial_\omega \hat{t}[n, k]| > 1^{-10} \\ G[n, k] & \text{otherwise} \end{cases}. \tag{58}$$

Eventually, the STET result can be obtained as

$$Te^{[2]}[n, k] = \begin{cases} G^{[2]}[n, k], & \text{if } |n - \hat{t}^{[2]}[n, k]| < \frac{T}{2}. \\ 0, & \text{otherwise} \end{cases}. \tag{59}$$

4. Numerical signal analysis

In this section, the performance of the proposed STET in dealing with noise contaminated signals is examined. A defect signal with impulse components as described in Ref. [30,31] is used in this simulation:

$$s(t) = \sum_{k=1}^K e^{\frac{-\zeta_0}{\sqrt{1-\zeta_0^2}} [2\pi f_0(t-T_k-\tau_0)]^2} \cos(2\pi f_0(t-T_k-\tau_0)) \tag{60}$$

where $K = 12$, damping ratio $\zeta_0 = 0.002$, central frequency $f_0 = 300$, time index $\tau_0 = 0.01$. The time-shift variable considering a random slip $T_k = 0.1(k + 0.05 \times \Delta T)$ where ΔT is a random value between 0 and 1. The time waveform and the STFT result of the signal are plotted in Fig. 4(a-b). The STET result and the zoomed version are shown in Fig. 4(c-d). It is obvious

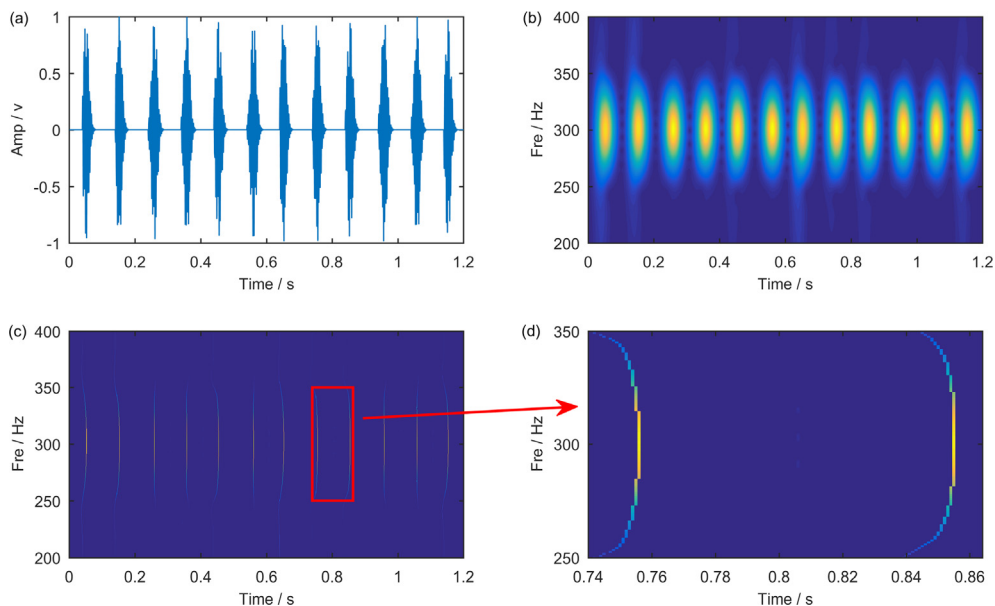


Fig. 4. (a) The time waveform of the signal given in Eq. (60), (b) STFT result, (c) STET result and (d) the zoomed version of the STET result.

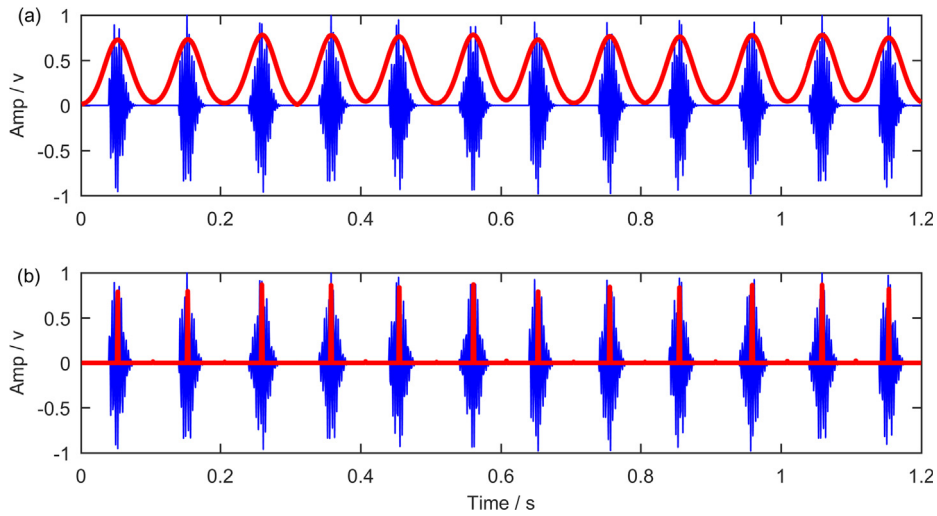


Fig. 5. (a) The slice of the STFT result at 300 Hz and (b) the slice of the STET result at 300 Hz.

from the figure that the TFR generated by STET has a much higher energy concentration than that of STFT. Considering that the central frequency of the simulated signal is 300 Hz, the slices of the TFRs from STFT and STET at 300 Hz, i.e. $|G(t, \omega)|_{\omega=2\pi 300\text{Hz}}$ and $|Te(t, \omega)|_{\omega=2\pi 300\text{Hz}}$ (the red color lines) are plotted in Fig. 5 together with the time waveform of the originally simulated signal (the blue color lines) for comparison. It is shown that the slice of the STET result at 300 Hz is highly concentrated and can exactly indicate the occurrence time instant of each impulse component. This property is very helpful in practice for accurately identifying the occurrence when a rolling element strikes the fault position of a bearing system.

In the following analysis, a Gaussian white noise is added onto the signal given in Eq. (60) and the waveform is plotted in Fig. 6(a). The STFT and STET results are shown in Fig. 6(b-d). It is observed that STET can still provide a good TFR in the presence of the noise interference. The slices of the STFT and STET results are plotted in Fig. 7 to further exemplify the performance of the STET in the analysis of noise contaminated signals. For sake of comparison, the TFRs generated by WT, RM, TSST and high-order SST from the same noise-added signal are shown in Fig. 8. It is worth noting that the Gaussian window function is used in all of these transforms. The slices of these four TFRs at 300 Hz are plotted in Fig. 9 together with the original

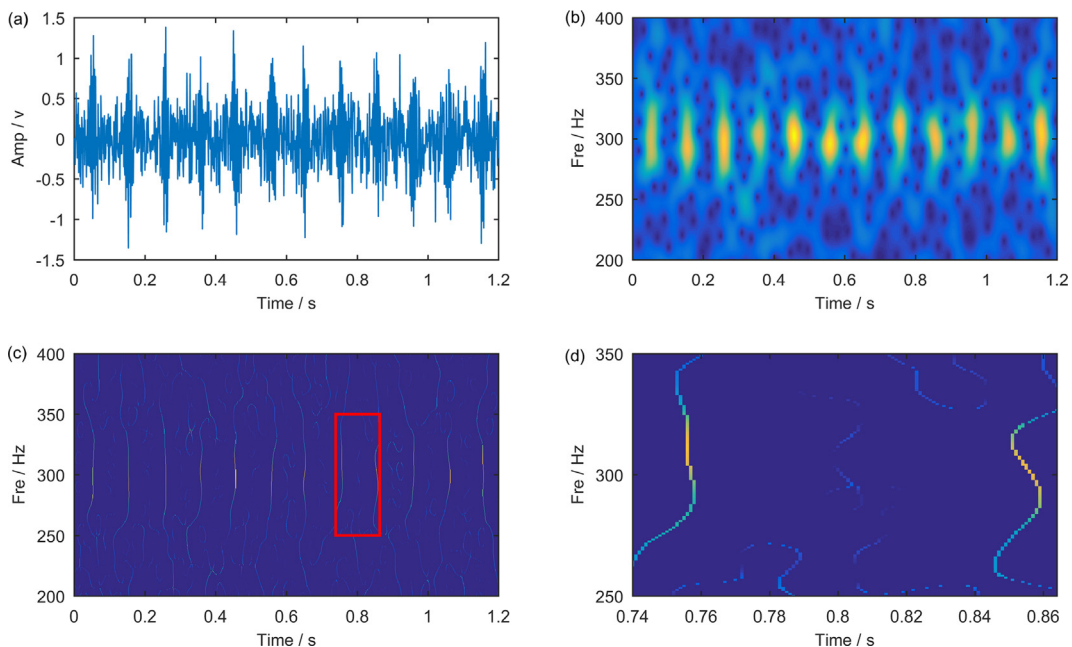


Fig. 6. (a) The waveform of the noise added signal, (b) STFT result, (c) STET result and (d) the zoomed version of the STET result.

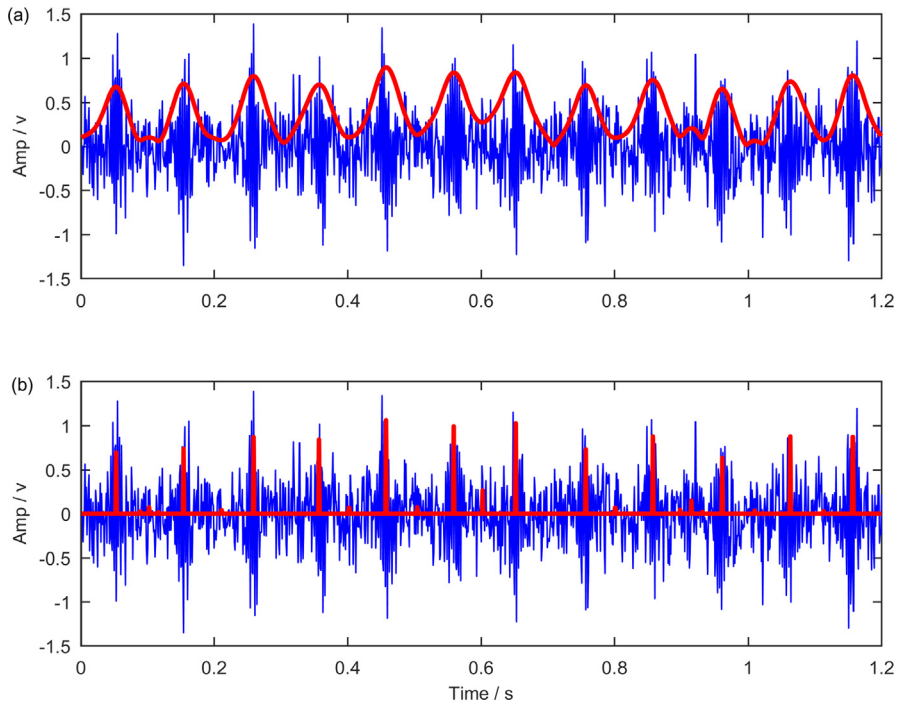


Fig. 7. (a) The slice of the STFT result at 300 Hz and (b) the slice of the STET result at 300 Hz.

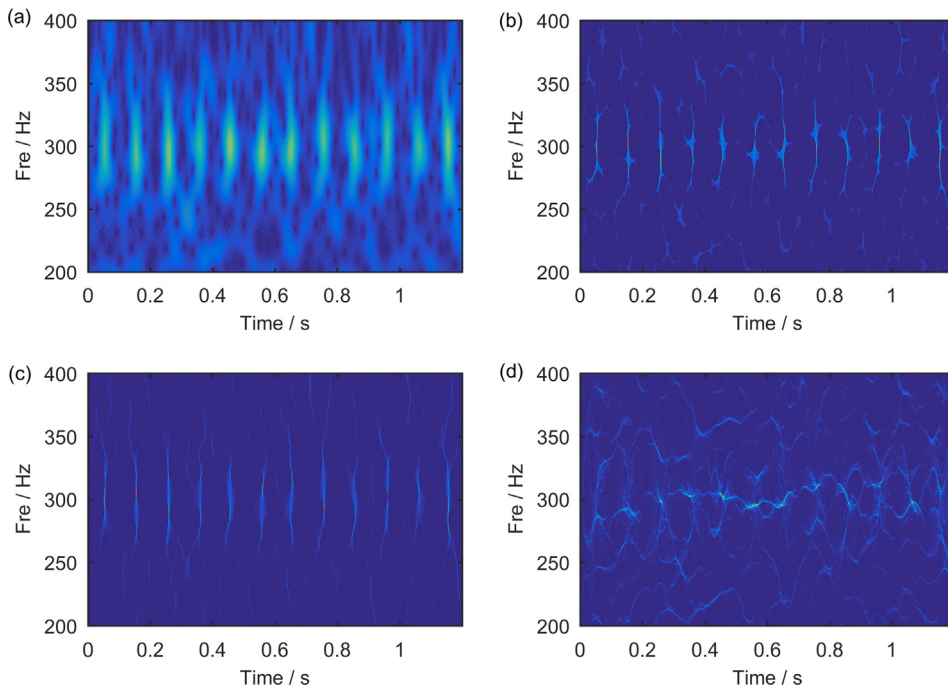


Fig. 8. (a) WT result, (b) RM result, (c) TSST result and (d) high-order SST result.

simulated signal. It is shown that the performance of the four TFA techniques is secondary comparing to that of the proposed STET technique.

To further exemplify the benefit of the proposed technique, bilinear transform techniques such as Wigner-Ville distribution (WVD), smoothed pseudo WVD (SPWVD), interference-reduced distribution with Bessel kernel (IRD-BK) and

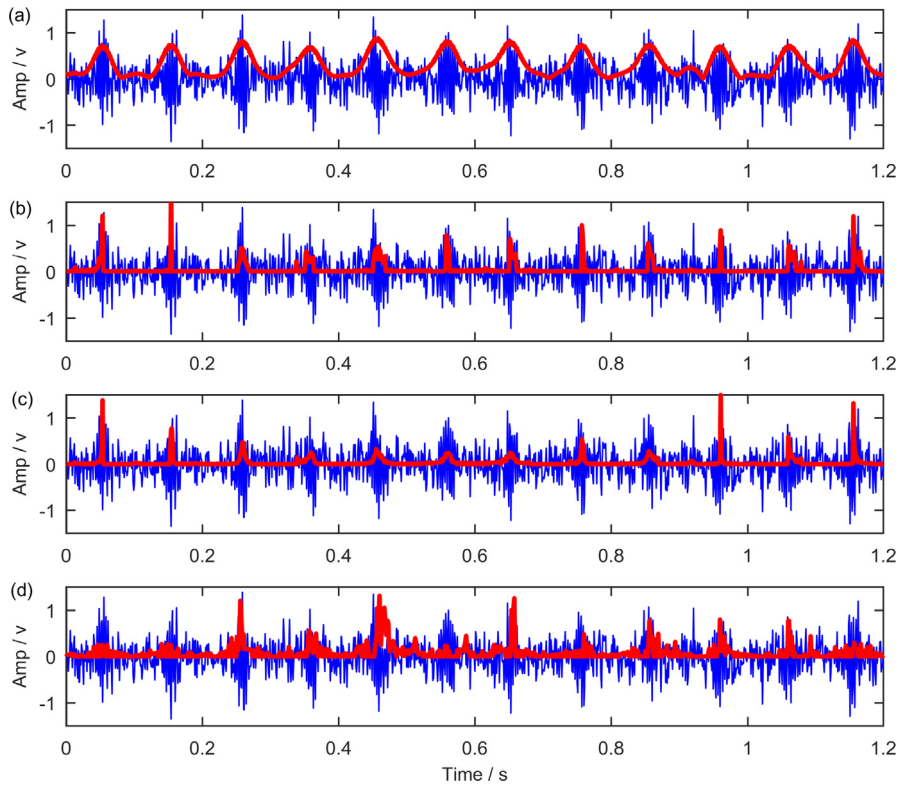


Fig. 9. The slices of (a) WT result, (b) RM result, (c) TSST result and (d) high-order SST result.

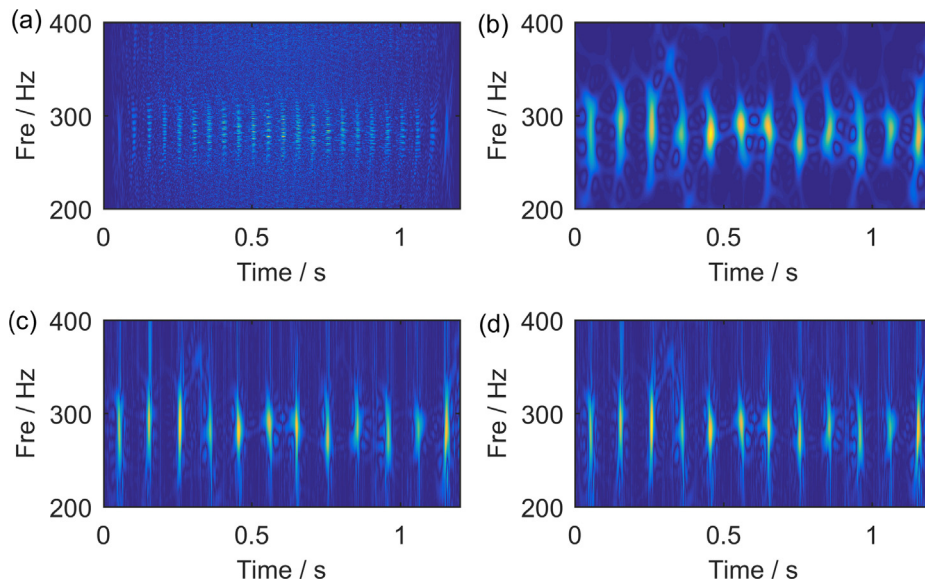


Fig. 10. The TFR of the noise added signal using (a) WVD, (b) SPWVD, (c) IRD-BK and (d) IRD-TK.

interference-reduced distribution with triangular kernel (IRD-TK) are also employed in the analysis of the noise-added signal and the TFA results are shown in Fig. 10 for comparison. It is shown that WVD will produce a strong interference in the TFR due to the cross-terms in the transform. The interference is largely suppressed using SPWVD, though somewhat it also leads to blurry TF energy distribution. Both IRD-BK and IRD-TK algorithms can enhance the energy concentration comparing to

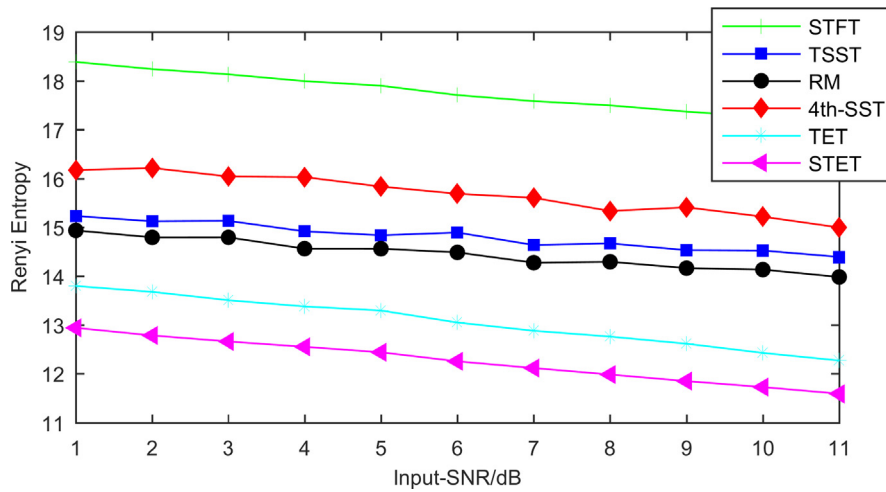


Fig. 11. Rényi entropy of different TFA methods for signals having different SNR levels.

that of SPWVD, though the added noise during the analysis process also hinders the characterization of impulsive-like features in the analysis of the noise-added signal (60).

The performance of the TFA methods in the analysis of the noise contaminated signal having various SNR levels is quantitatively compared using the Rényi entropy as shown in Fig. 11 where a lower Rényi entropy value denotes a more concentrated TFR. The Rényi entropy of order α for a TFR is defined as,

$$R^\alpha = \frac{1}{1-\alpha} \log_2 \frac{\int \int TFR(t, \omega)^\alpha dt d\omega}{\int \int TFR(t, \omega) dt d\omega} \quad (61)$$

where the order is usually set at $\alpha = 3$. It is shown that the proposed STET algorithm can achieve the most energy concentrated TFR for the simulated impulsive-like signal for all SNR levels.

The computer execution time of different TFA algorithms are listed in Table 2 to further evaluate the computation efficiency of the proposed algorithm in the analysis of the noise-added signal. It is shown that the executive time of the proposed STET is in the same scale to that of other TFA algorithms though the TFR energy concentration of the signal using the proposed technique is much higher than that of other TFA techniques.

The proposed STET algorithm is very sensitive to the impulse features contained in the signal. To verify this remark, two noise added signals are analyzed below where the kurtosis value, a widely accepted indicator in bearing fault diagnosis is used to demonstrate the effectiveness of the proposed technique to accurately extract the impulse components from signals containing various levels of noise interference. A random noise shown in Fig. 12(a) is used in this analysis. The sampling frequency of the signal is 1024 Hz and the sampling time is 1 s. The TFRs of the signal produced by STFT and the proposed algorithm are shown in Fig. 12(b-c) for comparison. It is shown that the TF features of the noise signal using STFT are widely spread in the entire TF plane. On the contrary, a highly energy concentrated impulse feature can be obtained using the proposed algorithm. Fig. 12(d) shows the reconstructed signal originated from the proposed algorithm. The calculated kurtosis values of the signals depicted by Fig. 12(a) and 12 (d) are 0.3037 and 6.9983 respectively. The result confirms that the proposed algorithm can substantially enhance the impulse features of a noise signal for a more accurate fault detection.

To further illustrate the effectiveness of the proposed algorithm in the analysis of noise contaminated signals, the technique is applied to analyze a noise added signal having two harmonic components shown in Fig. 13(a). The TFRs of the signal produced by STFT and the proposed algorithm are shown in Fig. 13(b-c). Fig. 13(d) shows the corresponding reconstructed signal originated from the proposed algorithm. The calculated kurtosis values of the signals shown in Fig. 13(a) and 13(d) are 0.1513 and 13.8881 respectively. The result confirms that the proposed algorithm can also be effectively employed to extract the impulse features from a non-impulsive signal.

Moreover, the change of the kurtosis value of the reconstructed signal from STET for the two-component signal under the influence of added noise with various SNR levels is shown in Fig. 14 together with that of the original noise added signal. It is shown that the reconstructed signal originated from the proposed analysis has much higher kurtosis value than that of the

Table 2

A comparison of the computer execution time using different algorithms.

Algorithm	STFT	TET	TSST	STET	RM	WT	High-order SST
Time (s)	0.069	0.245	0.829	0.58	0.423	0.483	2.45

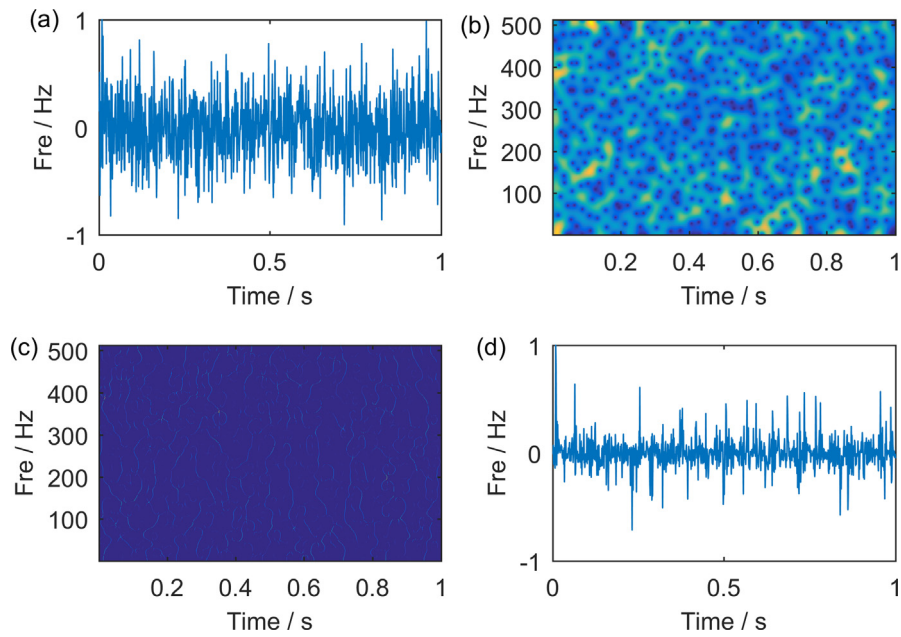


Fig. 12. (a) The waveform of a random noise signal, (b) STFT result, (c) STET result and (d) the reconstructed signal using STET.

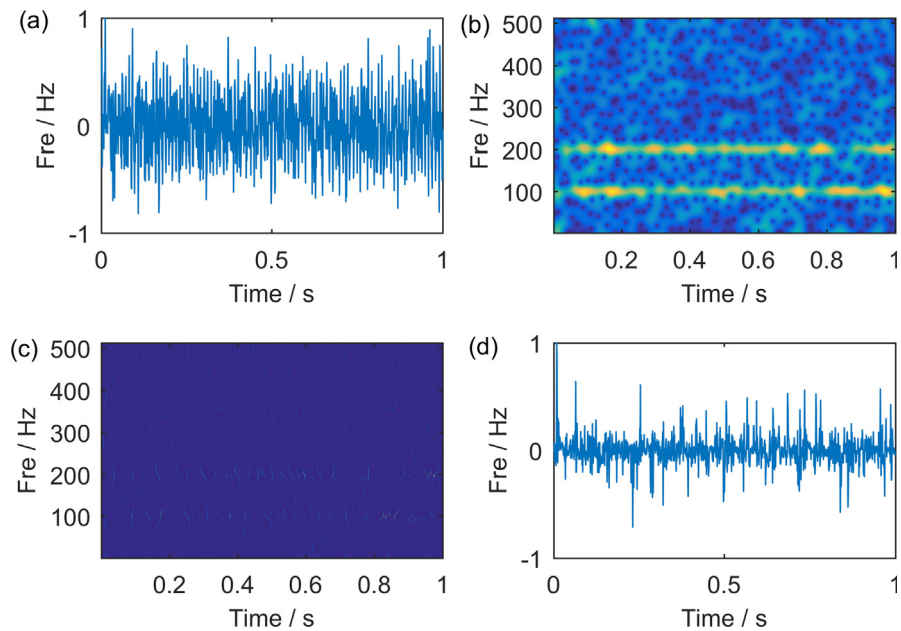


Fig. 13. (a) The waveform of the noise added harmonic signal, (b) STFT result, (c) STET result and (d) the reconstructed signal using STET.

original regardless of the SNR level, this implies the proposed technique can be effectively employed in dealing with signals having harmonic components and contaminated by strong noise.

5. Experimental validations

5.1. A bearing outer race fault of a rotating machine

Fig. 15 shows the bearing test rig used by Case Western Reserve University for simulated bearing fault experiments, which consists of an electric motor, a torque transducer and a dynamometer [32]. An artificial bearing outer race fault is sim-

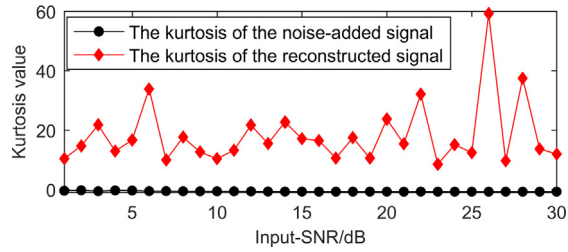


Fig. 14. A comparison of the kurtosis value of the reconstructed signal from STET and the original noise-added signal having various SNRs.

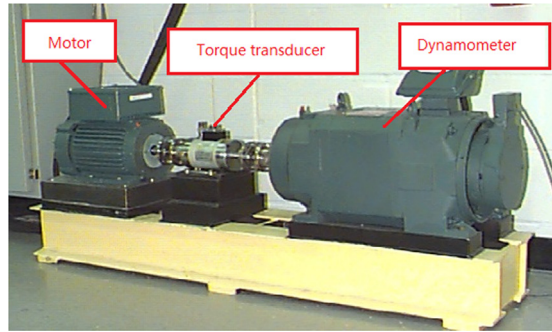


Fig. 15. The structural sketch of the machine.

ulated using the electro-discharge machine. Vibration signal is acquired by accelerometers placed at the drive end of the motor housing. Fig. 16(a) shows the waveform of the vibration signal. The shaft rotating speed of the machine is 1772 rpm. According to the bearing parameters provided by the manufacturer, the ball passing frequency of the bearing outer race is 105.877 Hz and the time interval between two successive impulses is 9.4 ms. It is seen from Fig. 16(a) that the time waveform of this signal exhibits the impulse feature caused by the bearing fault. However, it is difficult to deter-

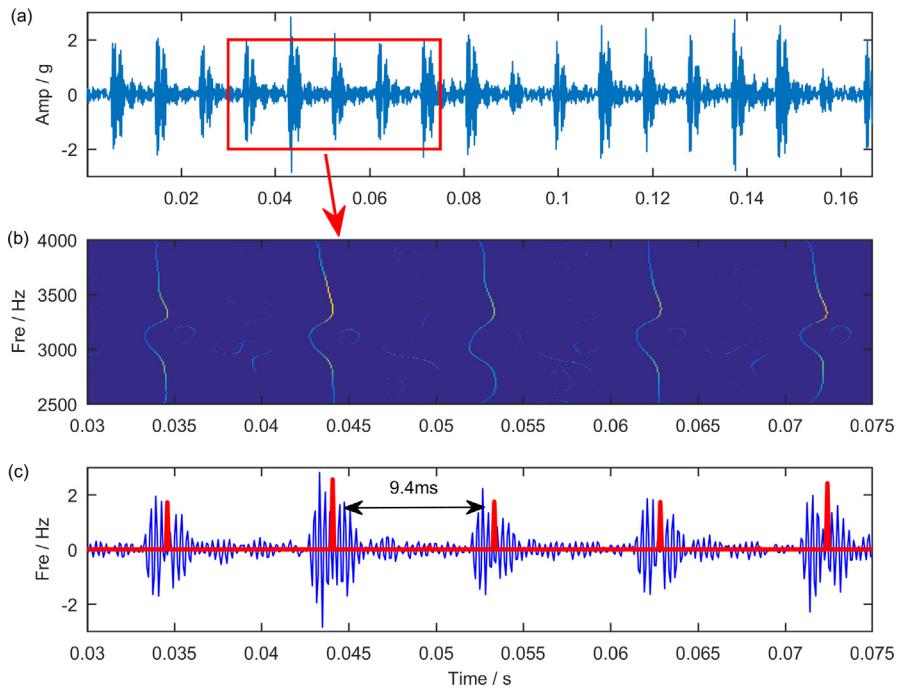


Fig. 16. (a) The time waveform of the bearing defect signal, (b) STET result and (c) the slice of the STET result.

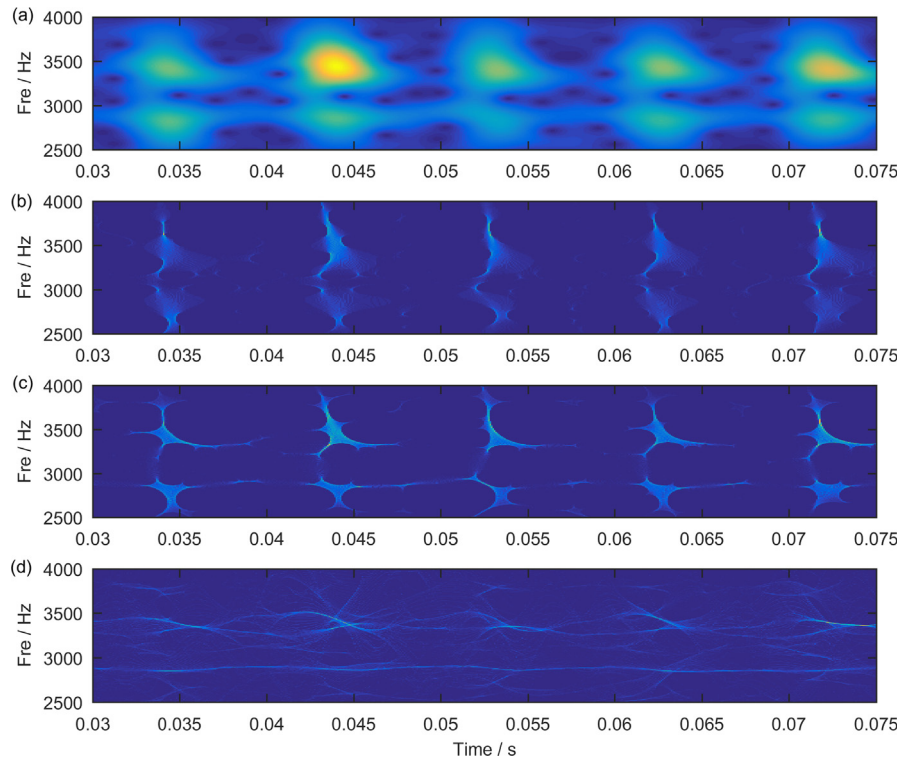


Fig. 17. (a) STFT result, (b) TSST result, (c) RM result and (d) high-order SST result.

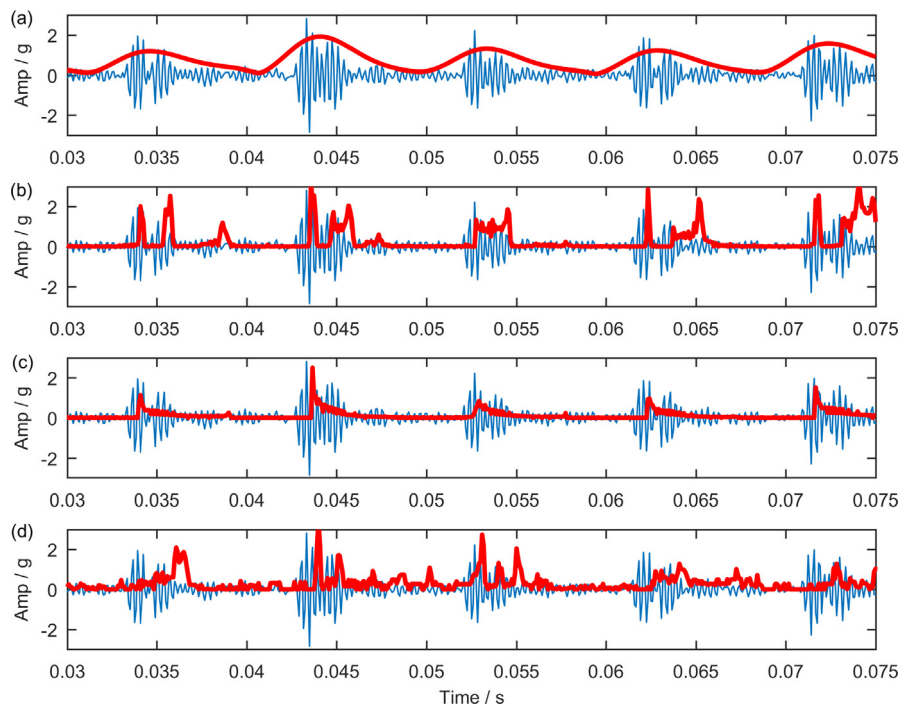


Fig. 18. The slices of the (a) STFT result, (b) TSST result, (c) RM result and (d) high-order SST result.

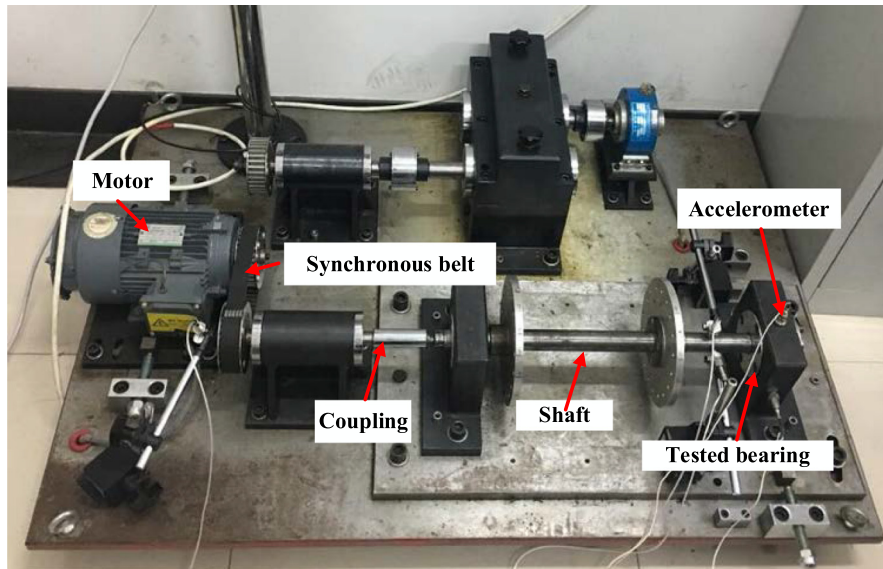


Fig. 19. The structural sketch of the machine.

mine the exact time instant when the impulse occurs from the time waveform. To address this problem, STET is used to extract the TF feature from this vibration signal as shown in Fig. 16(b). Fig. 16(c) shows the slice (the red color line) of the STET result at the frequency point 3336 Hz together with the original vibration signal (the blue color line). It can be observed that the slice can accurately capture the exact time instant of the occurrence of the impulses in the signal. The time interval captured by the STET analysis also matches well with the theoretical value. For comparison, this vibration signal is also analyzed by STFT, TSST, RM and high-order SST and the results are shown in Fig. 17. It is shown that none of them can

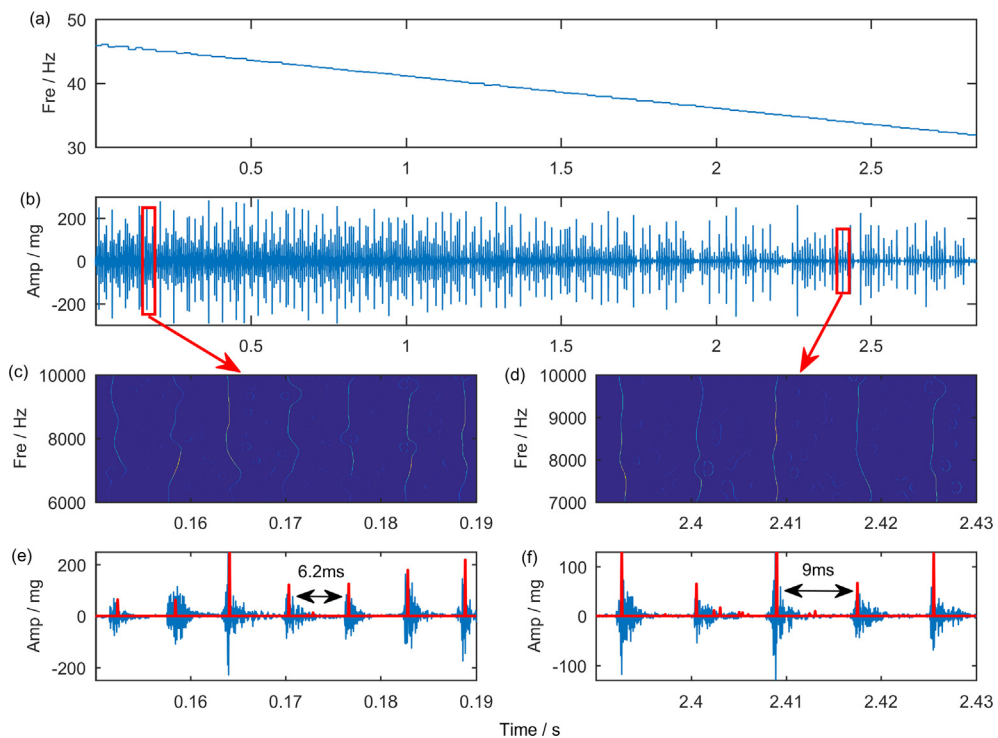


Fig. 20. (a) The RF, (b) waveform of the vibration signal, (c) STET result during 0.15 s–0.19 s, (d) STET result during 2.39 s–2.43, (e) the slice of the STET result and (f) the slice of the STET result.

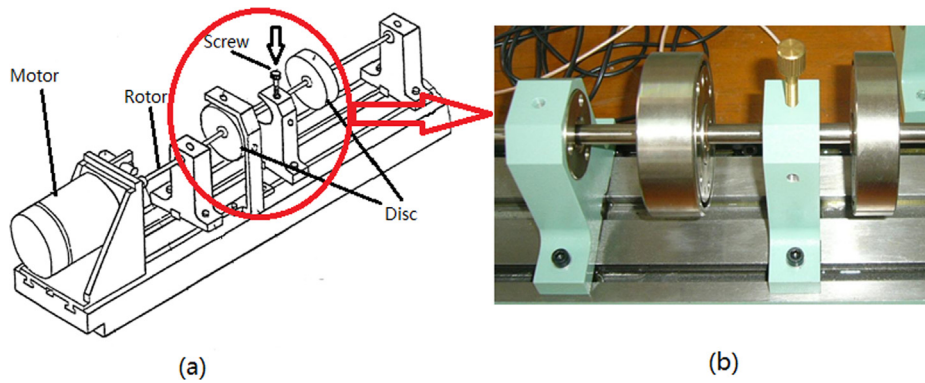


Fig. 21. (a) A schematic illustration of the test rig, (b) a graphical illustration of the test rig.

produce a highly concentrated TFR similar to that of the STET. Moreover, Fig. 18 shows that the slices of these TFRs cannot capture the exact time instant for the impulse component in the signal.

5.2. A bearing outer race fault of a rotating machine under varying operation speed

In this section, a bearing defect signal under varying speed condition is analyzed to further exemplify the effectiveness of the proposed technique. The signal is acquired from a machine test rig as shown in Fig. 19. The tested bearing is a type SKF 6205 bearing where an artificial fault is seeded in the outer race by wire cutting. An accelerometer is mounted on the bearing housing in the experiment. The normalized fault characteristic frequency (FCF) of the outer race with respect to the rotating frequency (RF) of this bearing is 3.583. The shaft RF decreases from 46 Hz to 30.7 Hz within 3 s during the test. The measured RF profile and the corresponding vibration signal are plotted in Fig. 20(a-b). STET is used to analyze two 40 ms signal segments (respectively, 0.15 s–0.19 s and 2.39 s–2.43 s) of the vibration signal and the TFRs are shown in Fig. 20(c-d). The TFRs display seven impulses and five impulses for the two signal 40 ms segments which highlights the speed varying condition of the machine. To accurately determine the fault type, the slices of the two TFRs are plotted in Fig. 20(e-f). From Fig. 20(a), the instantaneous values of the RF at 0.17 s and 2.41 s are found to be 45 Hz and 31 Hz respectively. The FCFs at these two time instants are 111.1 Hz and 161.28 Hz and the corresponding intervals between two successive impulses should be 6.2 ms and 9 ms. It can be observed from the Fig. 20(e-f) that the time intervals characterized by the slices of these two TFRs match well

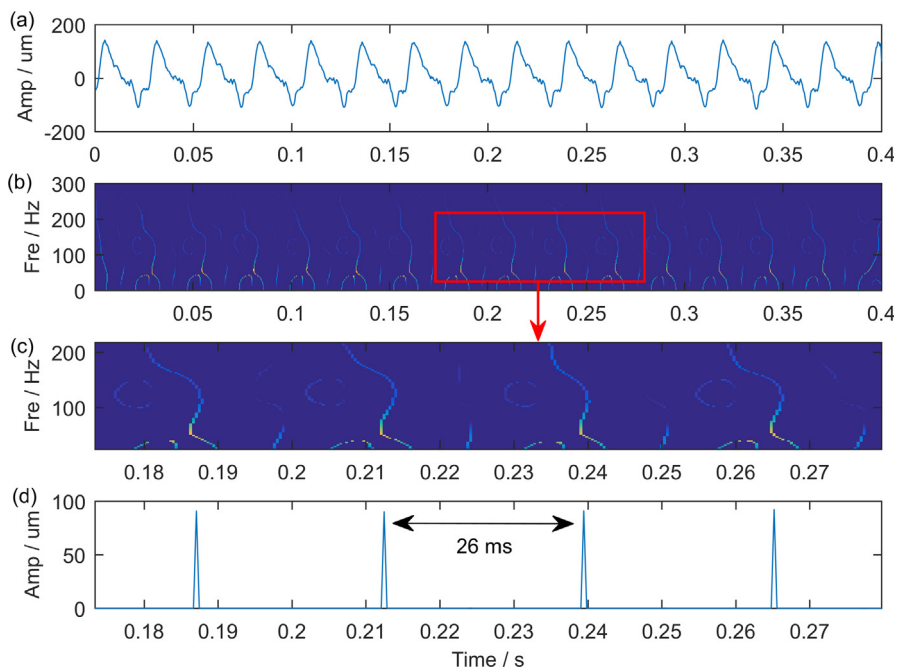


Fig. 22. (a) The waveform of the vibration signal, (b) STET result, (c) the zoomed version of the STET result and (d) the slice of the STET result.

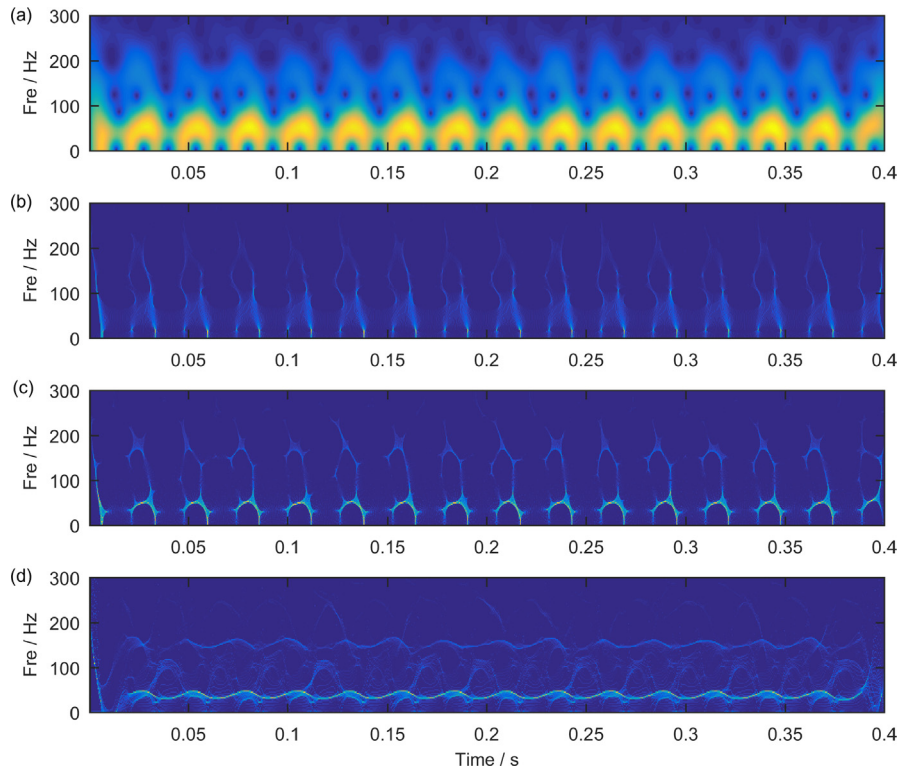


Fig. 23. (a) STFT result, (b) TSST result, (c) RM result and (d) high-order SST result.

with the theoretical values for both signal segments. This example highlights the effectiveness of the proposed technique in fault diagnosis of bearings under varying speed condition.

5.3. A rub impact fault of a rotating machine

In this section, the proposed technique is employed to analyze the signal of a rub impact fault of a rotating machine [33]. The structural sketch of the machine test rig is shown in Fig. 21. The vibration of the test rig is acquired by a displacement sensor, where the sampling frequency is 2560 Hz and the sampling time is 0.4 s. The shaft rotating speed during the experiment is 2295 rpm, which corresponds to the RF of 38.25 Hz. The rub impact is introduced by tightening the screw above the rotor. The time waveform of the vibration signal is shown in Fig. 22(a), which reveals limit fault information. STET is then employed to analyze this signal and the TFR is shown in Fig. 22(b-c). It is shown that impulse features can be clearly observed within the frequency interval between 0 Hz–200 Hz. According to Refs. [34–41], the impulse caused by the rub impact between the rotor and the screw should happen once for each rotation. Considering that the current RF is 38.25 Hz, which means that the interval between two successive impulses should be 26.1 ms. A slice of the TFR at the frequency 82.5 Hz is plotted in Fig. 22(d). It is shown that the slice from the TFR using the proposed technique can precisely capture the occurrence time instant of the rub impact between the rotor and the screw. This confirms that the proposed technique can be employed to capture the impulse like signals generated by a rub impact. For comparison, the TFRs of the rub impact signal using STFT, TSST, RM and high-order SST are shown in Fig. 23. It becomes obvious that these TFR techniques cannot yield the accurate features and are difficult to extract the exact features required for the detection of the rub impact fault.

6. Conclusion

A high resolution TFA method termed as STET was proposed in this paper in the analysis of the impulsive-like signals for machine fault diagnosis. The proposed technique was developed based on a second-order frequency-varying model which has the capacity to handle noise contaminated signals and non-stationary impulse signals from real-world applications. Both the 2D GD estimate bias and the amplitude bias of STFT caused by the second-order model are rectified under the framework of the STET. Moreover, a discrete algorithm is implemented in the study by calculating various alternative STFTs. The effectiveness of the proposed STET technique was verified using a number of numerical simulated signals and three sets of experimental data. The results confirm that the technique proposed in the study has the capacity to produce a highly energy-

concentrated TFR even for strong frequency-varying signals under a strong noisy interference environment and varying speed conditions. The analysis results from this study highlight the potential applications of the proposed technique in condition monitoring and fault diagnosis of rotating machinery. A MATLAB implementation of the proposed algorithm is available at <https://ww2.mathworks.cn/matlabcentral/fileexchange/77398>.

CRedit authorship contribution statement

Gang Yu: Conceptualization, Methodology, Validation, Writing - original draft, Writing - review & editing. **Tian Ran Lin:** Conceptualization, Formal analysis, Supervision, Writing - review & editing.

Declaration of Competing Interest

The authors declare that they have no known competing financial interests or personal relationships that could have appeared to influence the work reported in this paper.

Acknowledgments

This work was supported by National Natural Science Foundation of China under Grant 61901190, and Shandong provincial key research project under the Grant No 2018GGX109011.

References

- [1] T.R. Lin et al, A simple signal processing approach for condition monitoring of low speed machinery using Peak-Hold-Down-Sample algorithm, *Mech. Syst. Signal Process.* 36 (2013) 256–270.
- [2] S. Wang, X. Chen, C. Tong, Z. Zhao, Matching synchrosqueezing wavelet transform and application to aeroengine vibration monitoring, *IEEE Trans. Instrum. Meas.* 66 (2017) 360–372.
- [3] S. Wang, X. Chen, I.W. Selesnick, et al, Matching synchrosqueezing transform: A useful tool for characterizing signals with fast varying instantaneous frequency and application to machine fault diagnosis, *Mech. Syst. Signal Process.* 100 (2018) 242–288.
- [4] W. Huang, G. Gao, N. Li, et al, Time-frequency squeezing and generalized demodulation combined for variable speed bearing fault diagnosis, *IEEE Trans. Instrum. Meas.* 68 (2018) 2819–2829.
- [5] X. Tu, Y. Hu, F. Li, et al, Demodulated high-order synchrosqueezing transform with application to machine fault diagnosis, *IEEE Trans. Indust. Electron.* 66 (2018) 3071–3081.
- [6] X. Zhu, Z. Zhang, J. Gao, et al, Two robust approaches to multicomponent signal reconstruction from STFT ridges, *Mech. Syst. Signal Process.* 115 (2019) 720–735.
- [7] Y. Guan, M. Liang, D.S. Neculescu, Velocity synchronous linear chirplet transform, *IEEE Trans. Ind. Electron.* 66 (2018) 6270–6280.
- [8] Y. Guan, M. Liang, D.S. Neculescu, Velocity synchronous bilinear distribution for planetary gearbox fault diagnosis under non-stationary conditions, *J. Sound Vib.* 443 (2019) 212–229.
- [9] Z.K. Peng, G. Meng, F.L. Chu, Z.Q. Lang, W.M. Zhang, Y. Yang, Polynomial chirplet transform with application to instantaneous frequency estimation, *IEEE Trans. Instrum. Meas.* 60 (2011) 1378–1384.
- [10] Y. Yang, Z.K. Peng, X.J. Dong, et al, General parameterized time-frequency transform, *IEEE Trans. Signal Process.* 62 (2014) 2751–2764.
- [11] S. Mann, S. Haykin, The chirplet transform: Physical considerations, *IEEE Trans. Signal Process.* 43 (1995) 2745–2761.
- [12] X. Li, G. Bi, S. Stankovic, et al, Local polynomial Fourier transform: A review on recent developments and applications, *Signal Process.* 91 (2011) 1370–1393.
- [13] S. Wang, X. Chen, G. Cai, B. Chen, X. Li, Z. He, Matching demodulation transform and synchrosqueezing in time-frequency analysis, *IEEE Trans. Signal Process.* 62 (2014) 69–84.
- [14] F. Auger, P. Flandrin, Improving the readability of time-frequency and time-scale representations by the reassignment method, *IEEE Trans. Signal Process.* 43 (1995) 1068–1089.
- [15] F. Plante, G. Meyer, W.A. Ainsworth, Improvement of speech spectrogram accuracy by the method of reassignment, *IEEE Trans. Speech Audio Process.* 6 (1998) 282–287.
- [16] G. Thakur, E. Brevdo, N.S. Fućkar, et al, The synchrosqueezing algorithm for time-varying spectral analysis: Robustness properties and new paleoclimate applications, *Signal Process.* 93 (2013) 1079–1094.
- [17] Z. He, X. Tu, W. Bao, et al, Gaussian-modulated linear group delay model: application to second-order time-reassigned synchrosqueezing transform, *Signal Processing* 107275 (2019).
- [18] G. Yu et al, Synchroextracting transform, *IEEE Trans. Ind. Electron.* 64 (2017) 8042–8054.
- [19] Z. Li, J. Gao, Z. Wang, A time-synchroextracting transform for the time-frequency analysis of seismic data, *IEEE Geosci. Remote Sens. Lett.* (2019).
- [20] J. Tao, C. Qin, C. Liu, A synchroextracting-based method for early chatter identification of robotic drilling process, *Int. J. Adv. Manuf. Technol.* 100 (2019) 273–285.
- [21] Z. Li, J. Gao, H. Li, et al, Synchroextracting transform: The theory analysis and comparisons with the synchrosqueezing transform, *Signal Process.* 166 (2020) 107243.
- [22] T. Oberlin et al, Second-order synchrosqueezing transform or invertible reassignment? Towards ideal time-frequency representations, *IEEE Trans. Signal Process.* 63 (2015) 1335–1344.
- [23] D.H. Pham et al, High-order synchrosqueezing transform for multicomponent signals analysis—With an application to gravitational-wave signal, *IEEE Trans. Signal Process.* 65 (2017) 3168–3178.
- [24] J. Shi, M. Liang, D.-S. Neculescu, Y. Guan, Generalized stepwise demodulation transform and synchrosqueezing for time-frequency analysis and bearing fault diagnosis, *J. Sound Vib.* 368 (2016) 202–222.
- [25] K. Yu, T.R. Lin, H. Ma, et al, A combined polynomial chirplet transform and synchroextracting technique for analyzing nonstationary signals of rotating machinery, *IEEE Trans. Instrum. Meas.* 69 (2020) 1505–1518.
- [26] Y. Hu, X. Tu, F. Li, High-order synchrosqueezing wavelet transform and application to planetary gearbox fault diagnosis, *Mech. Syst. Signal Process.* 131 (2019) 126–151.
- [27] K. Yu, H. Ma, H. Han, et al, Second order multi-synchrosqueezing transform for rub-impact detection of rotor systems, *Mechanism and Machine Theory* 140 (2019) 321–349.
- [28] D. He et al, Time-reassigned synchrosqueezing transform: The algorithm and its applications in mechanical signal processing, *Mech. Syst. Signal Process.* 117 (2019) 255–279.

- [29] G. Yu, A concentrated time-frequency analysis tool for bearing fault diagnosis, *IEEE Trans. Instrum. Meas.* 69 (2020) 371–381.
- [30] R. Randall et al, Rolling element bearing diagnostics—A tutorial, *Mech. Syst. Signal Process.* 25 (2011) 485–520.
- [31] W. Fan et al, Sparse representation of transients in wavelet basis and its application in gearbox fault feature extraction, *Mech. Syst. Signal Process.* 56 (2015) 230–245.
- [32] W.A. Smith, R.B. Randall, Rolling element bearing diagnostics using the Case Western Reserve University data: A benchmark study, *Mech. Syst. Signal Process.* 64 (2015) 100–131.
- [33] G. Chen, "Vibration data of a rotating machinery with fault" [Online]. Available: <http://ides.nuaa.edu.cn>.
- [34] P. Zhou, M. Du, S. Chen, et al, Study on intra-wave frequency modulation phenomenon in detection of rub-impact fault, *Mech. Syst. Signal Process.* 122 (2019) 342–363.
- [35] X. Zhu, Z. Zhang, J. Gao, et al, Synchroextracting chirplet transform for accurate IF estimate and perfect signal reconstruction, *Digital Signal Process.* 93 (2019) 172–186.
- [36] K. Yu, H. Ma, J. Zeng, et al, An amplitude weak component detection technique based on normalized time-frequency coefficients and multi-synchrosqueezing operation, *Measure. Sci. Technol.* 30 (2019) 055008.
- [37] S. Wang, X. Chen, G. Li, X. Li, Z. He, Matching demodulation transform with application to feature extraction of rotor rub-impact fault, *IEEE Trans. Instrum. Meas.* 63 (2014) 1372–1383.
- [38] S. Chen, M. Du, Z.K. Peng, et al, High-accuracy fault feature extraction for rolling bearings under time-varying speed conditions using an iterative envelope-tracking filter, *J. Sound Vib.* 448 (2019) 211–229.
- [39] S. Chen, Y. Yang, Z.K. Peng, et al, Detection of rub-impact fault for rotor-stator systems: A novel method based on adaptive chirp mode decomposition, *J. Sound Vib.* 440 (2019) 83–99.
- [40] G. Yu, Z. Wang, P. Zhao, Multisynchrosqueezing transform, *IEEE Trans. Ind. Electron.* 66 (2019) 5441–5455.
- [41] G. Yu, Z. Wang, P. Zhao, Z. Li, Local maximum synchrosqueezing transform: An energy-concentrated time-frequency analysis tool, *Mech Syst. Signal Process.* 117 (2019) 537–552.